

The Progress Of SPP Oxidation In Zircaloy-4 And Its Relation To Corrosion And Hydrogen Pickup

James Sayers^a, Sergio Lozano-Perez^{a*1}, Susan R. Ortner^b

^a Department of Materials, University of Oxford, Parks Road, Oxford OX1 3PH

^b National Nuclear Laboratory, Culham Science Centre, Abingdon, Oxon OX14 3DB

¹ Corresponding author.

e-mail address: sergio.lozano-perez@materials.ox.ac.uk

Abstract

The evolution of Cr and Fe within the oxide formed on Zircaloy-4 in high-temperature pure water and a high-pH aqueous environment has been followed in detail by electron energy loss spectroscopy (EELS). The oxidation states of Cr, Fe and Zr have been determined as a function of exposure time and location in the oxide film. Much Cr and all the Fe diffuse out of the original Laves phase and precipitate within cracks or on the outer oxide surface. Cr oxidation is complete prior to transition; Fe oxidation occurs mainly after transition. The different hypotheses concerning the mechanisms by which the alloying elements influence oxidation and hydrogen pickup are examined in the light of this information. The mechanisms which agree with these observations include: doping of the bulk ZrO_2 by low levels of aliovalent cations; doping ZrO_2 grain boundaries with aliovalent cations; injection of holes into near-surface oxide by islands of Fe_2O_3 ; reaction of water with islands of metallic Fe (and Ni) on surfaces of internal cracks around transition; control of transition by mechanical properties

Key Words

Oxidation, SPP, Zircaloy-4, STEM, EELS,

1. Introduction

Zirconium alloys were selected in the late 1940s for structural components in the fuel assemblies of nuclear reactors with water coolants due to their neutron transparency and their anticipated ability to withstand corrosion at high temperatures and maintain integrity under irradiation [1]. In the decades since, precise compositions and processing routes have been modified continuously to reduce corrosion in primary water, minimise the associated pickup of hydrogen and to reduce radiation-induced dimensional changes [2] [3] [4]. Early in the development of the Zr-Sn alloys (Zircalloys), additions of the transition elements Cr, Fe and Ni were found to delay the onset of high, linear corrosion rates [5] [6]. These elements have very low solubility in the Zr-Sn matrix, so are present as second phase particles (SPPs) predominantly $\text{Zr}(\text{Cr,Fe})_2$ in Zircaloy-4, with some Zr_2Fe . For a range of Zr-Cr/Ni/Fe binary alloys and Zircaloy-4, the uniform corrosion rate in high temperature water was found to decrease as the SPP volume fraction and precipitate size increased [7], although nodular corrosion was encouraged by large SPP sizes [8]. Decreasing the Fe:Cr ratio in $\text{Zr}(\text{Cr,Fe})_2$ has been found to decrease the oxidation rate [9], but increase the hydrogen pickup fraction [10].

A number of mechanisms have been suggested whereby SPP-forming elements affect oxidation or hydrogen pickup, involving different oxidation states and locations for the solutes. For example, the SPPs in Zircaloy-4 are more noble than the matrix so, when SPP and matrix are in electrical contact with each other and the environment, the SPPs provide cathodic sites and remain metallic [11]. While the SPPs remain metallic and the oxide is thinner than the SPP diameter, the SPPs could act as short-circuit metallic conduction paths across the insulating oxide [12] [13] [14]. When the SPPs oxidise, the alloying elements tend to migrate out of the original SPP bounds, partitioning to islands rich in Fe and Cr. If Fe migrates out of oxidising SPPs and forms linked metallic islands, these also could provide high conductivity paths. Even if the solute elements oxidise, interlinked regions of iron and chromium oxides might still provide a somewhat higher conduction path than the highly-insulating zirconia [15]. Less simplistically, it has been suggested that, in the outermost regions of the oxide film, where the oxygen concentration is high enough to make the oxide a p-type semiconductor [16], then a layer of Fe_2O_3 could inject electron holes into the nearby ZrO_2 , increasing its conductivity [6] [17] – a mechanism which would decrease conductivity in n-type oxide nearer the metal-oxide interface. Finally, if the solute elements are not clustered, but distributed as alliovalent cations on the Zr sites, then they can affect the anion site vacancy concentrations or form complexes with the relatively doubly-charged anion vacancies [18] [19] [20] [21] affecting their mobility. The presence of alliovalent cations can also affect the space charge across the oxide and, hence, the energy barriers for diffusion-migration [12] [22] [23]. Alliovalent cations in oxide grain boundaries have also been suggested to act as hydrogen ion recombination sites, suppressing hydrogen pickup [24].

The various mechanisms proposed differ significantly in the state in which they assume the alloying elements to exist. It should, therefore, be possible to assess the applicability of the mechanisms to oxidation and hydrogen pickup by examining the actual states of the alloying elements as the alloy oxidises. Different types of SPP oxidise at different rates, either at the same time as the surrounding matrix, or over some distance from the metal-oxide interface [15] [25] [26] [27] [28] [29]. This is partly related to the nature of the SPP as a whole, with delayed oxidation observed for SPPs with smaller free energies of oxidation (ΔG smaller than -760kJ/mol of oxygen) [25]. It also reflects the nature of the individual elements and their partitioning into different regions as the SPP oxidises [15]

[25] [26] [27] [28] [29], with higher oxygen potentials required to oxidise Nb, Cr, Fe and Ni than Zr [30]. Kinetic factors may also be significant, both with respect to the partitioning and with respect to the oxidation of the different products of partitioning. Experimental investigations are, therefore, required to characterise the oxidation state and distribution of alloying elements across the oxide layer as a function of oxide thickness, and to help clarify whether various proposed contributions of alloying elements are viable. Since SPPs tend to be both sparse and small, it has proved difficult to acquire statistically meaningful, spatially-resolved information on the oxidation states of precipitate-forming elements. This work uses a detailed STEM/EELS (scanning transmission electron microscopy with electron energy loss spectroscopy) study to characterise the oxidation of the second phase particles as a function of oxide thickness and SPP location in Zircaloy-4 to underpin mechanistic understanding of alloying element effects. The majority SPP in Zircaloy-4 is Zr(Fe,Cr)_2 . In order to derive statistically meaningful trends in oxidation behaviour, this study has focussed on the oxidation behaviour of Fe and Cr in these SPPs. The plausibility of the different hypotheses concerning the roles of SPPs in oxidation and hydrogen pickup are then assessed in the light of the trends observed.

2. Methods

Zircaloy-4 sheet (Zr-1.31Sn-0.20Fe-0.11Cr-0.13O % by weight, 9 wt. ppm H) was provided by Westinghouse. Some corrosion coupons 25mm x 70 mm x 0.5 mm were exposed in a static autoclave at Amec Foster Wheeler (now Wood plc). The corrosion environment was 50% heavy water, containing 2 wt. ppm Li, 95 wt. ppm wt. K and 1050 wt. ppm B, deaerated with nitrogen at room temperature, then raised to 350°C ($\text{pH}_{350} = 8.82$). The autoclave was emptied and refreshed and the samples weighed every 5-30 days. Other corrosion coupons were exposed to pure water at 360°C ($\text{pH}_{360} = 6.15$) by Westinghouse Electric Company in accordance with ASTM G2 [31]. The weight gains were converted to average oxide thicknesses using a conversion factor of $15.0\mu\text{g}/\text{dm}^2 = 1\mu\text{m}$ [13].

Samples were prepared for STEM/EELS using the focussed ion beam miller (FIB) in-situ lift-out method [32] using a FEI FIB200 for initial lift-out and a Zeiss NVision FIB-SEM for thinning to electron transparency until a thickness of ~50nm was reached. STEM and EELS were carried out on a cold field emission source JEOL ARM-200F, with an acceleration voltage of 200kV. High-angle annular dark field (HAADF) images were obtained with two JEOL ADF detectors (located before the viewing screen) and a Gatan ADF (located just before the EELS spectrometer). EELS data were acquired with a Gatan Quantum GIF spectrometer, with 2048 channels. The SPPs were examined using core loss EELS. Given that all SPPs analyzed were over 100nm in diameter and the matrix Fe and Cr content are very low, the data have been analysed assuming that the signal originated predominantly at the SPPs.

There are several methods of determining the oxidation state of a metal using EELS [33] [34] [35] [36] [37]. The difference between the onset of the O K-edge and the onset of the L_3 -edge for the transition metal increases when the oxidation state of the metal increases. Using this difference to assess the oxidation state of the Fe and Cr will be referred to as the $\Delta E(\text{Fe})$ or $\Delta E(\text{Cr})$ method in the following. The ratio of the areas in the L_3 and L_2 peaks also increases with oxidation (the L_3/L_2 method), while the full width half maximum (FWHM) of the L_3 peak narrows. The FWHM method, however, is only reliable in the absence of multiple scattering events and was not found to be

consistently reliable for the foils examined in this study. The oxidation state may also be assessed by measuring the ratio of O to metallic species from the peak areas.

3. Results

Figure 1 shows the range of oxide thicknesses produced in this work and identifies the oxide thicknesses at transition (defined in this case as the time mid-way between the last points clearly belonging to the first cycle and those clearly belonging to the second cycle of oxidation).

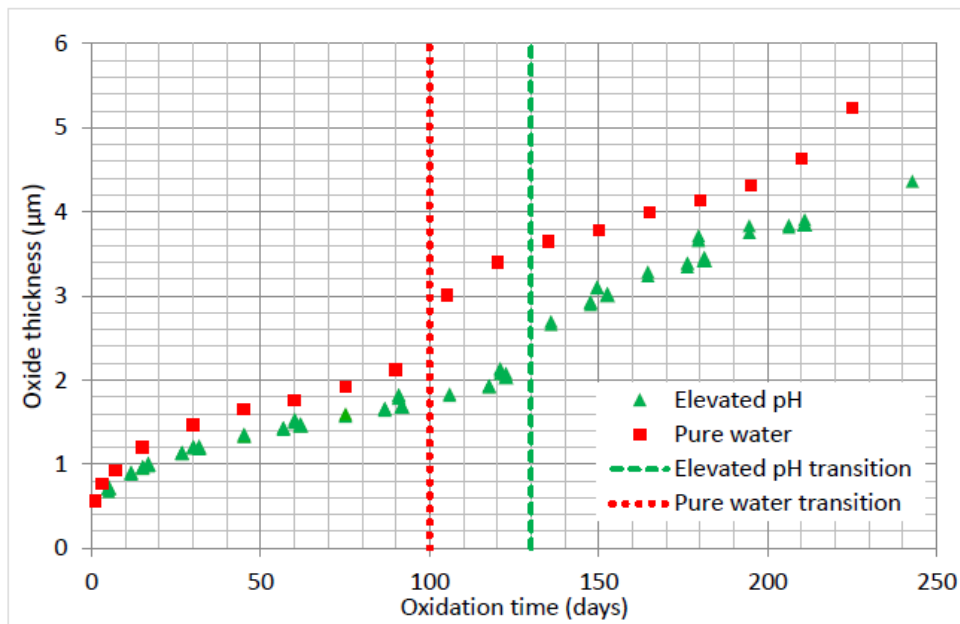


Figure 1. Oxidation of samples examined in this work

Figure 2 - Figure 9 and Table 1 - Table 4 show the morphologies, the detailed element distributions and oxidation state-related EELS parameters for a selection of SPPs in the metal and in the oxide at increasing distances from the metal oxide interface (MO). The environment was not found to affect the SPP oxidation rate as a function of oxide thickness [38], so the data are presented as a function of SPP distance from the MO alone without separating the results into subsets according to the environment. Figure 2 shows two SPPs within the metal substrate and the corresponding core-loss EELS spectrum showing the locations of the O K and Fe and Cr L peaks. The O K peak is small, resulting from surface oxidation of the foil. The light areas under each SPP result from the FIB milling. Several metallic SPPs were analysed. The Fe:Cr ratio in each was found to be even across the SPP, but there was some variation in the ratio between particles, with an average of 1.3.

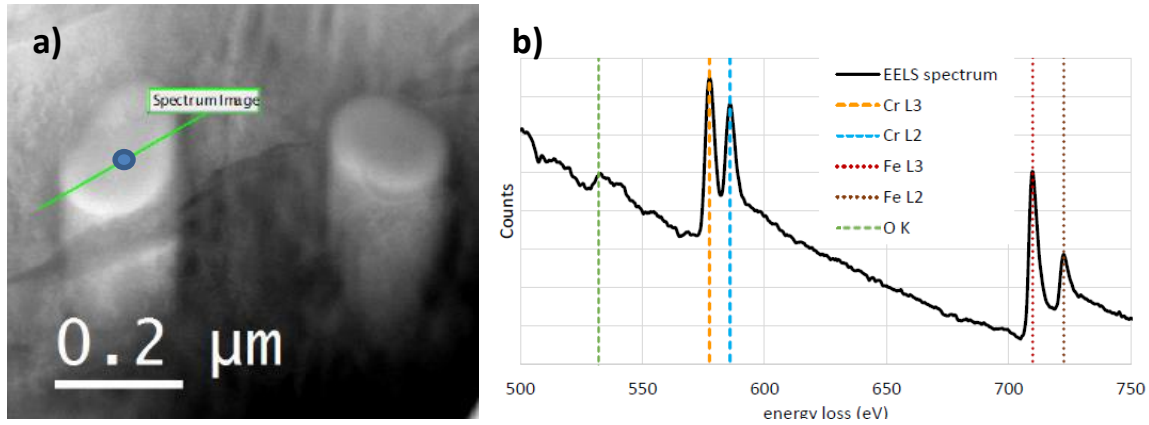


Figure 2. SPPs in metal substrate (a) HAADF image, with dashed green line to show location of line profile. (b) Example EELS spectrum from centre of SPP (indicated by the spot on the line profile), showing the location of edges for O, Cr and Fe.

Figure 3 shows an SPP at the MO of a 2.06 μm thick oxide. (This thickness is the average thickness defined by weight gain measurements on a sample exposed for 122d in the high pH environment). In this and all the following images, the oxide growth direction is downwards. Comparing the EELS spectra acquired at the edge of the SPP neighbouring the oxide and in the centre of the SPP (along the green dashed line) shows that the Zr at the edge of the SPP has begun to oxidise while that in the centre has not. The EELS parameters in Table 1 show that the Cr has also begun to oxidise at the SPP edge, while the Fe has not. The magnitudes of the L₂ and L₃ edges in Figure 3 also show that the ratio of Fe to Cr is lower at the edge of the SPP where oxidation has initiated than in the centre.

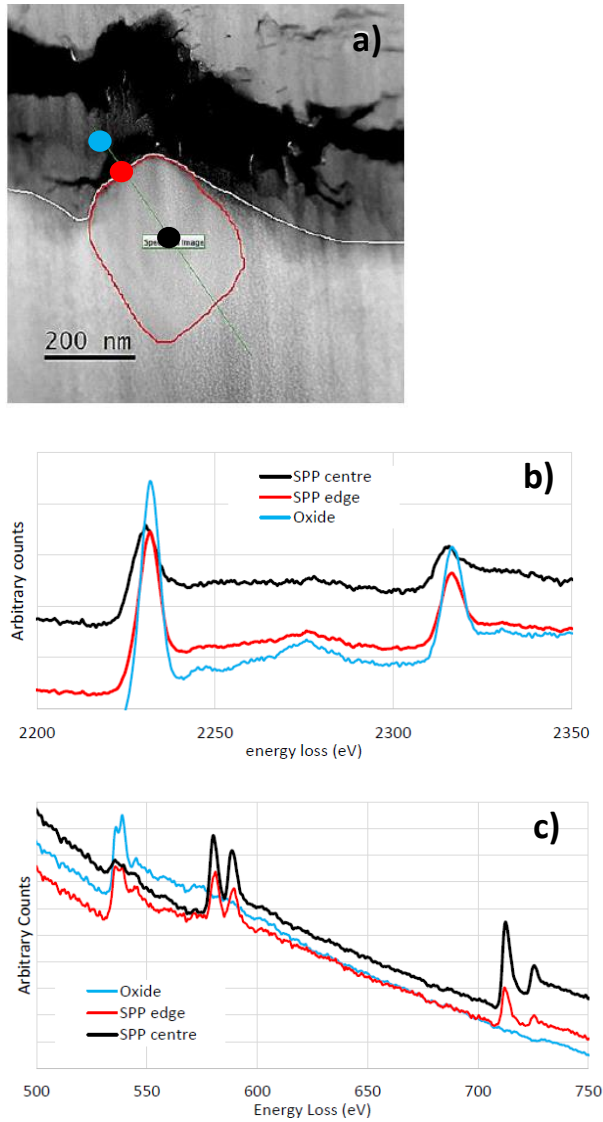


Figure 3 (a) HAADF image of SPP at metal-oxide interface of 2.06µm oxide, (b) Zr $L_{2,3}$ edges and (c) O K Cr $L_{2,3}$ and Fe $L_{2,3}$ edges. EEL spectra were extracted from the colour-coded points along the line profile in the image.

	Cr		Fe	
	Centre	Edge	Centre	Edge
ΔE (eV)	43.75	44.25	176.25	176.25
L_3/L_2	1.55	1.64	3.74	3.38

Table 1. Summary of the EELS parameters for Fe and Cr in the SPP at the interface of the 2.06µm oxide.

Figure 4 shows an SPP (or, rather, a pair of SPPs, given the protrusion on the left of the main SPP) which has just been submerged in oxide formed by exposure to pure water for 165 d i.e. with an average oxide thickness of 3.99 µm. There is a large crack above the SPP and smaller cracks below it, on the edge closer to the MO. The SPP lies between 40 nm and 290 nm from the MO which, on the basis of the oxidation rates shown in Figure 1, indicates that it has been exposed to oxide between approximately 15 s and 3 h. Even after such short exposures, there is clear evidence of O incorporated into the SPP. The Fe/Cr ratio ranges from 0.74 in the blue region of the heat map in

Figure 4c to 1.53 in the yellow region; the O/Fe ratio decreases from 13 to 0.84 in the same regions.

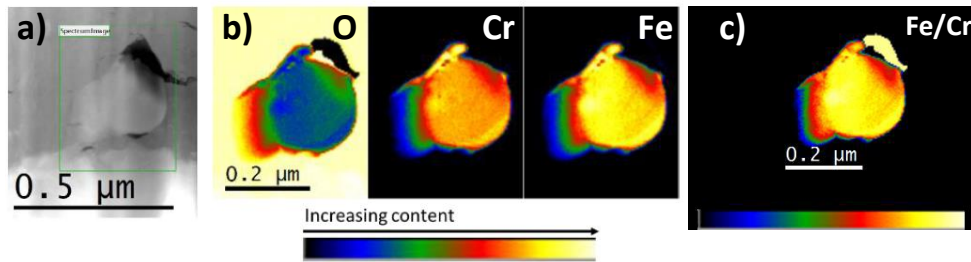


Figure 4 SPP 40nm from OM in a 3.99µm oxide film (a) HAADF image (b) heat maps for (from left to right) O, Cr and Fe contents (c) heat map for Fe/Cr ratio.

The EELS spectra shown in Figure 5 are coloured to show the locations in the Fe/Cr heat map (Figure 4c) from which they were acquired. For the Zr $L_{2,3}$ edges in Figure 5a, the edge in the blue spectrum (outer edge of left side of SPP) is at 2233eV, as is the edge in the bulk oxide, indicating that Zr^{4+} is present at the SPP rim. The Zr $L_{2,3}$ edge in the yellow spectrum (centre of SPP) is at 2231, as in the metal, indicating that Zr at the centre of the SPP (here around 80-250nm from the MO) remains metallic. The edges in the red and green regions are at 2231 and 2232 indicating an intermediate oxidation state (most likely a mixture of Zr^{0+} and Zr^{4+}) near the rim of the SPP. The Cr spectra indicate that the Cr may have oxidised slightly in the blue region, but the Fe spectrum does not show any change indicating oxidation. Note that the spectrum from the bulk oxide (purple line) confirms that negligible Cr and Fe signals derive from the bulk oxide.

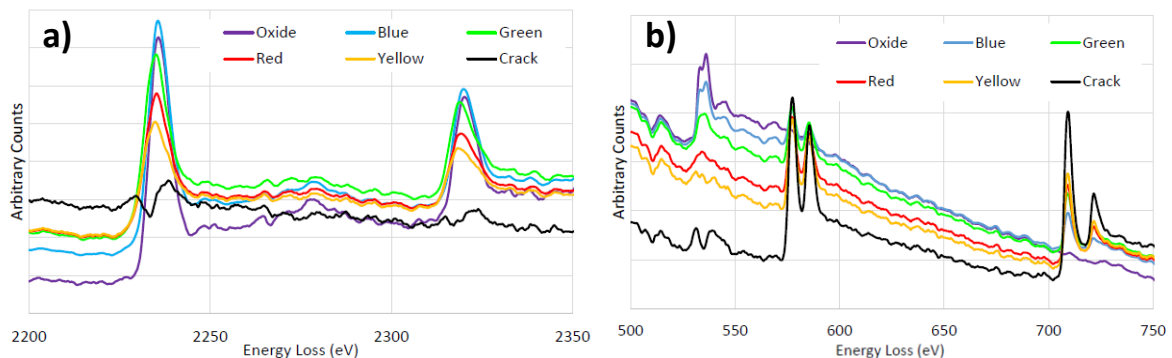


Figure 5. EELS spectra from SPP 40nm from OM in 3.99µm oxide, (b) Zr $L_{2,3}$ edges and (c) O K Cr $L_{2,3}$ and Fe $L_{2,3}$ edges.

Figure 5 shows an SPP located 330nm from the MO in an oxide 3.99µm thick formed in pure water. This SPP will have been exposed to oxide for between 5h (lower edge) and 31h (upper edge) during the second cycle of oxidation. A large crack has formed above the SPP and smaller cracks below it, closer to the interface. The inhomogeneous manner in which oxidation progresses is very clear. Oxygen has diffused into the SPP along internal cracks (or interfaces if this SPP is, like that in

Figure 4, actually a cluster of particles, but even the Zr in the central part of the SPP is clearly not fully oxidised. The Fe and Cr are both depleted in the high-O veins, and have now enriched within

the external crack. Throughout the SPP and crack, the Fe/Cr ratio is 1.2. Comparing the EELS spectra (Figure 7), from the bulk oxide, the high-O veins in the SPP, elsewhere within the original SPP bounds, and within the crack, shows that the Zr has begun to oxidise within the high-O vein, but not elsewhere. The EELS parameters (Table 2) show that neither the Cr nor the Fe has oxidised anywhere in or around the SPP. It should be noted that, although the cracks around some of the SPPs appear “hollow” in the HAADF images, EELS analysis reveals that they contain O, Cr and Fe. Their low density explains the low signal in the HAADF image.

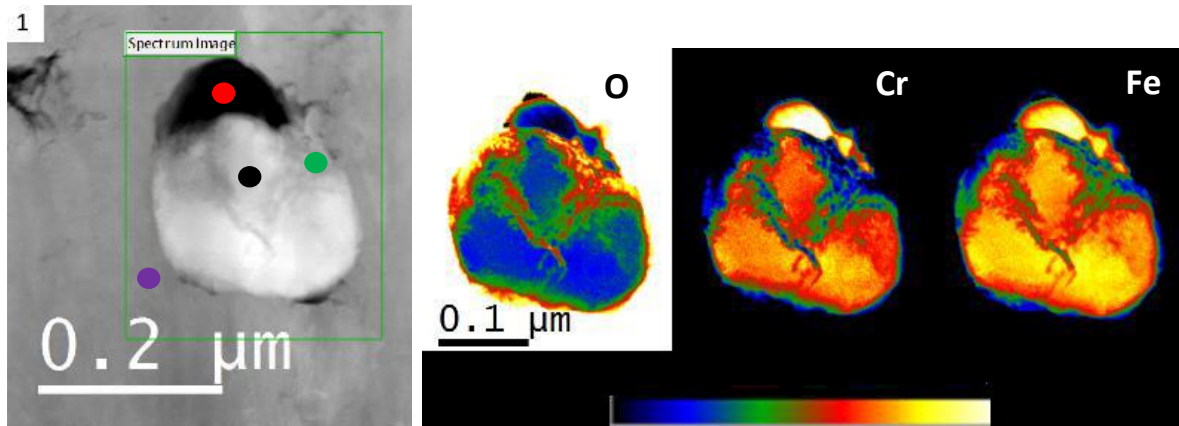


Figure 6. SPP 330nm from the MO in sample exposed to pure water 165d (average oxide thickness = 3.99μm). HAADF image (left) and corresponding heat maps (left to right) for O, Cr and Fe.

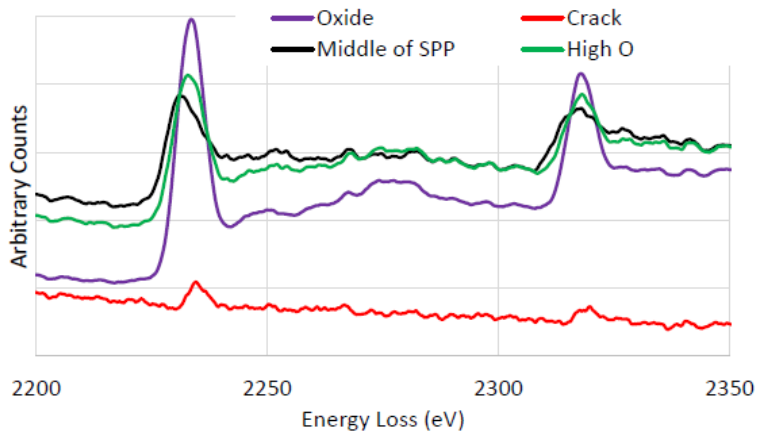


Figure 7. Zr spectra from different regions (see spots in Fig 6) in and around oxidising SPP 300nm from MO of 3.99μm oxide.

	Cr			Fe		
	Crack above SPP	Mid-SPP	High-O Vein	Crack above SPP	Mid-SPP	High-O vein
ΔE (eV)	43.75	43.5	43.5	175.25	175.25	175.25
L ₃ /L ₂	1.57	1.56	1.62	3.37	3.04	3.25

Table 2. Summary of the EELS parameters for Fe and Cr in and around the SPP 300nm from the MO of 3.99μm oxide.

Figure 8 shows an SPP lying 1.55μm from the MO of a sample exposed to high-pH water for 123d (average oxide thickness 2.08μm) which has been in contact with oxide for between ~64-85d. This shows the now characteristic appearance of uneven oxidation within the original bounds of the SPP;

Fe and Cr part-filling the crack capping the oxidised SPP; uneven Cr distribution within the original SPP bounds and the crack. The Fe has now been expelled fully from within the original SPP bounds and is filling the crack above the SPP. Because so much Fe has now been expelled from the original SPP bounds, the crack is now more completely filled and the intensity in the HAADF is much higher than in earlier images (E.g. Fig 6). In this and all following SPPs, the Zr has oxidised fully throughout the SPP.

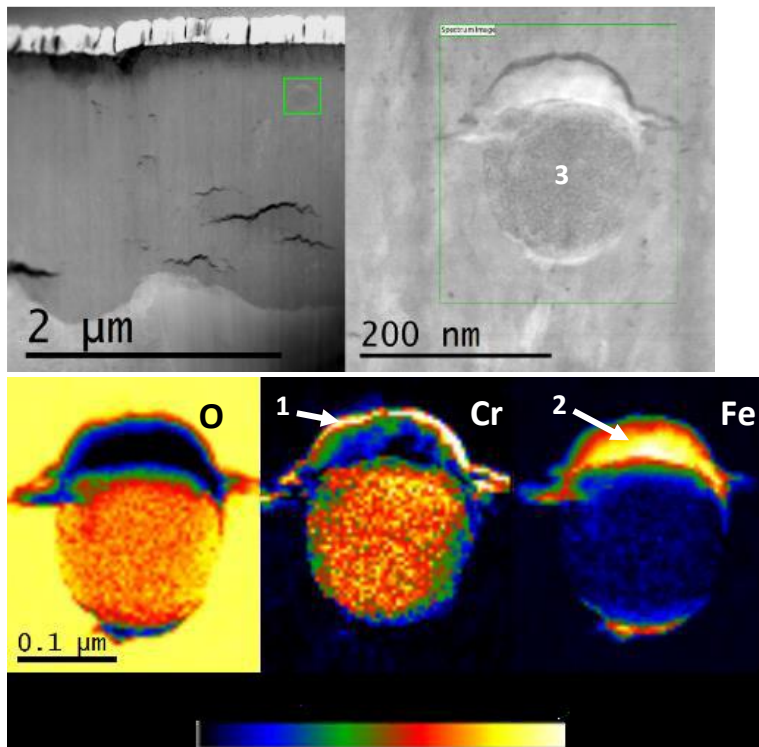


Figure 8. SPP 1.55μm from MO in sample exposed to high-pH water 123d (average oxide thickness = 2.08μm). HAADF general view (top left), HAADF showing SPP and map region (top right) and corresponding heat maps for O, Cr and Fe (bottom, left to right).

	Cr			Fe		
	High-Cr part of crack (1)	High-Fe part of crack (2)	Mid-SPP (3)	High-Cr part of crack	High-Fe part of crack	Mid-SPP
ΔE (eV)	44.75	44	44.75	-	176.5	-
L ₃ /L ₂	2.03	1.84	1.97	-	3.28	-

Table 3. Summary of the EELS parameters for Fe and Cr in and around the SPP 1.55μm from the MO of 2.08μm oxide.

Figure 9 shows an SPP 2.45μm from the MO of a sample exposed to high-pH water for 211d (average oxide thickness 3.86μm). This SPP is, thus within the fossil oxide and has been in contact with oxide between 132-147d. The central part of the SPP is oxidised, Fe and Cr are unevenly enriched in cracks above and below the SPP and Fe has been expelled from the SPP. Both the Fe and the Cr appear to have oxidised in this example, although in similar SPPs within the fossil oxide, the change in the Fe EELS spectra were smaller than shown here.

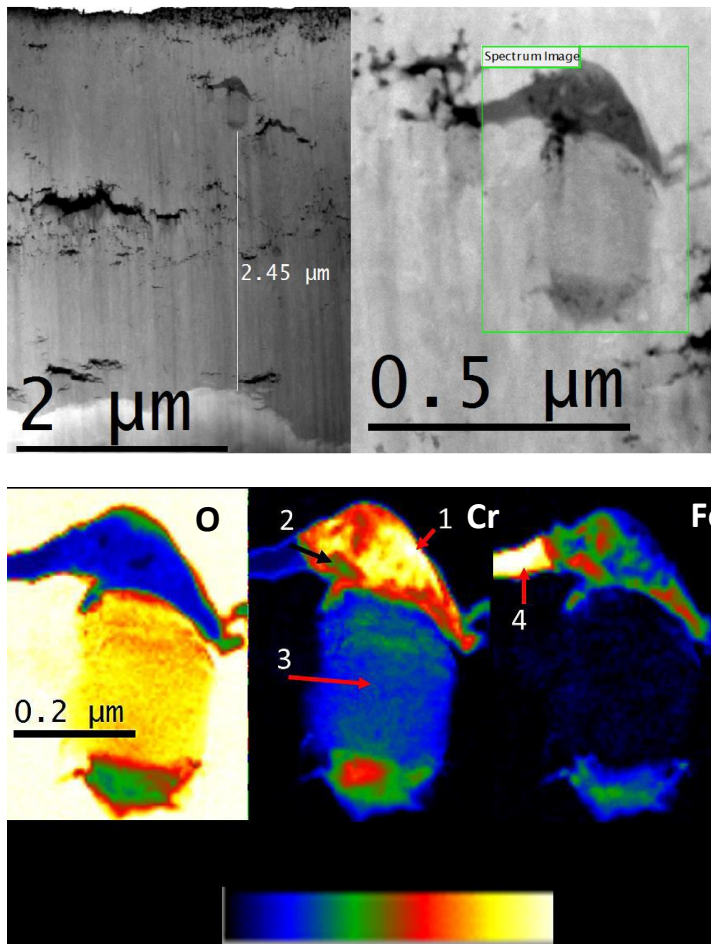


Figure 9. SPP 2.45μm from MO in sample exposed to high-pH water 211d (average oxide thickness = 3.86μm). HAADF general view (top left), HAADF showing SPP and map region (top right) and corresponding heat maps for (bottom, left to right) O, Cr and Fe.

	Cr				Fe	
	High-Cr part of crack (1)	Mixed part of crack (2)	High-Fe part of crack (4)	Mid-SPP (3)	Mixed part of crack (2)	High-Fe part of crack (4)
ΔE (eV)	44.75	44.75	-	44.75	176.75	176.75
L ₃ /L ₂	1.97	2.05	-	1.84	4.28	4.32

Table 4. Summary of the EELS parameters for Fe and Cr in and around the SPP 2.45μm from the MO of 3.86μm oxide.

These data may be summarised in terms of the behaviour of material remaining within the original bounds of the SPPs and the behaviour of material which collects outside the SPPs. Figure 10a shows the ratio of oxygen to Fe+Cr within SPPs at different distances from the metal-oxide interface. The oxide content in the middle of the SPPs increases progressively with distance from the interface. Any SPPs more than around 2.2μm from the metal-oxide interface will be in the fossil oxide, and it can be seen that the oxygen level inside the original SPP bounds has reached a stable level by this location.

The oxygen potential is expected to be fixed at the oxide-water interface (OW) and at the metal-oxide interface (MO). If the change in potential is linear across the oxide, then the potential will not

be constant at a given distance from the MO, but at a given fraction of the distance from the MO to the OW. Figure 10b therefore plots the SPP oxygen content as a function of the fractional distance from the MO. (In this plot, the fractional distance is defined as the distance to the MO, measured on the TEM foil, divided by the mean film thickness defined by the weight gain.) SPPs beyond $x=1$ in this representation are in the fossil oxide. A linear trend line ($R^2=0.86$) is drawn through the data from pre-transition specimens to guide the eye, clarifying that data from SPPs in thick and thin oxides align, which indicates that oxidation occurs in a similar way in first cycle and second cycle oxides. (Data from SPPs from both high pH and pure water environments are plotted.) The O content reflects the oxidation of Zr, Cr and Fe. Zr within the SPP has fully oxidised by the point at relative distance =0.4, so further increases in O are due to the oxidation of the alloying elements alone.

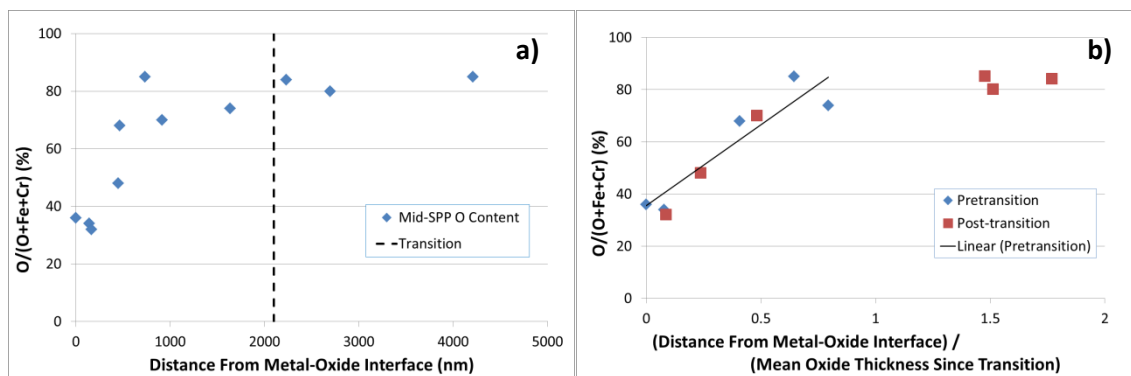


Figure 10. Oxygen content of SPPs (a) at different distances from the metal-oxide interface (b) at different fractions of the non-fossil oxide thickness.

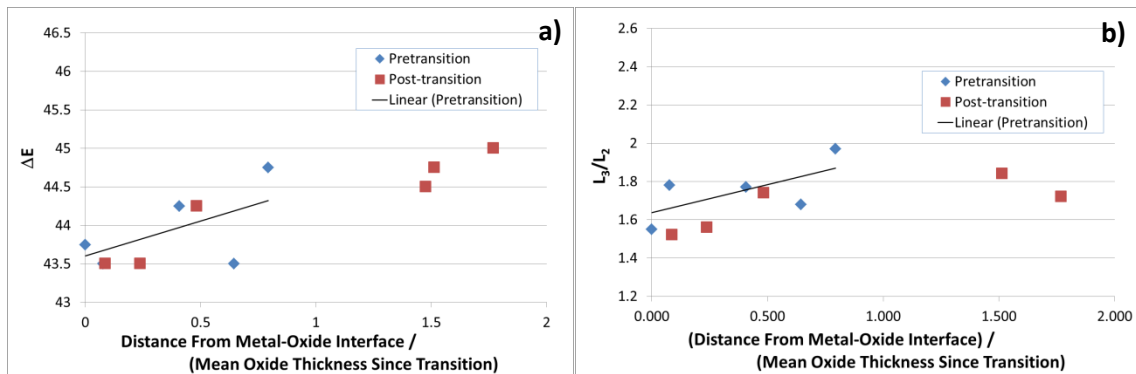


Figure 11. Change in oxidation state of Cr inside original bounds of SPPs at different locations within the oxide using (a) ΔE (in eV) (b) L_3/L_2 .

a)

b)

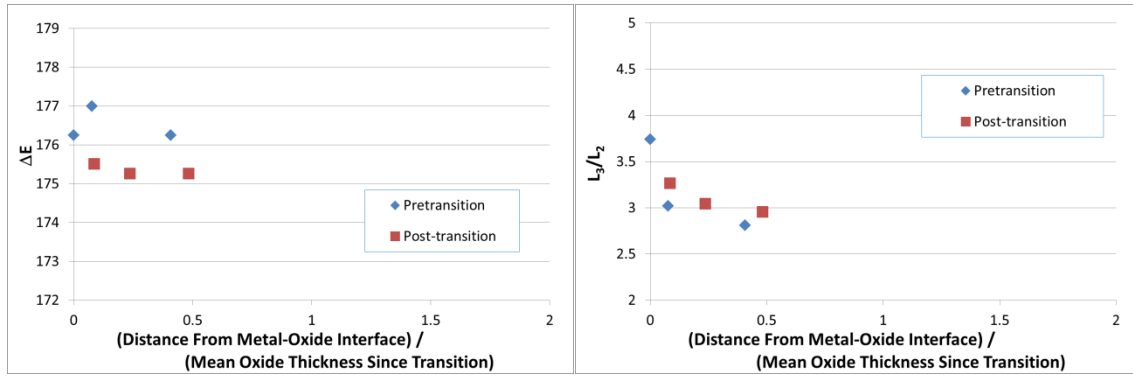


Figure 12 Change in oxidation state of Fe inside original bounds of SPPs within the oxide using (a) ΔE (in eV) (b) L_3/L_2 .

The behaviour of the alloying -SPP regions is summarised in Figure 11 - Figure 12. Trend lines are drawn in Figure 11 to indicate the mean behaviour of the pre-transition samples ($R^2=0.33$). Both ΔE and L_3/L_2 suggest that Cr has reached a stable oxidation state prior to transition. If the asymptotic levels of ΔE and L_3/L_2 indicate full oxidation, then the oxidation of Cr in the middle of SPPs is completed by the time the MO has advanced to leave the SPP more than three-quarters of the way across the current cycle oxide. There is no evidence that Fe oxidises before it migrates out of the original SPP bounds. Figure 13 shows the migration of Fe out of the middle of the SPP. The trend line ($R^2=0.73$) indicates that the Fe has migrated out of the middle of the SPP by the time the SPP is around two thirds of the way across the current cycle oxide.

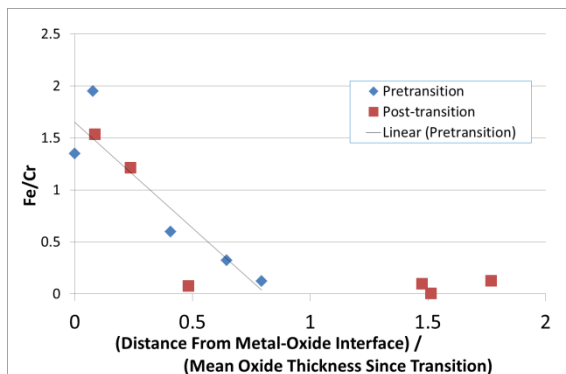


Figure 13 Ratio of Fe to Cr inside original SPP bounds at different locations in oxide

Figure 14 shows that the oxygen content of material which has moved out of the original SPP bounds and diffused to fill the cracks does not reach a stable level by transition. The oxygen level in the expelled material continues to increase even within the fossil oxide.

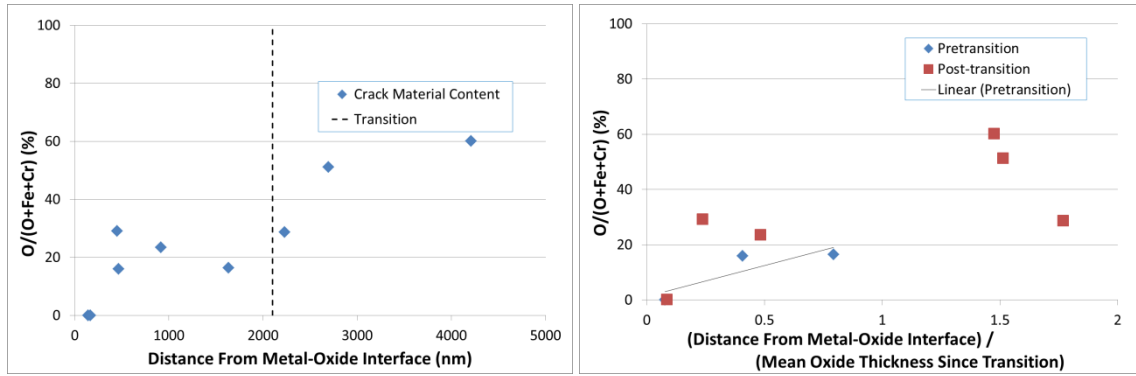


Figure 14 Relative oxygen content of material within cracks outside original SPP bounds at different locations within oxide.

Figure 15 shows that the expelled Cr in the Cr-rich regions of the crack reaches a stable oxidation state at about the same point (around $\frac{3}{4}$ of the way across the new oxide) as the Cr within SPP bounds. It is possible that Cr in the Fe-rich regions oxidises more slowly, but the different measures of oxidation do not show this consistently. The difference in oxygen content between the material inside and outside the original SPP bounds therefore seems dominated by the slower rate of Fe oxidation.

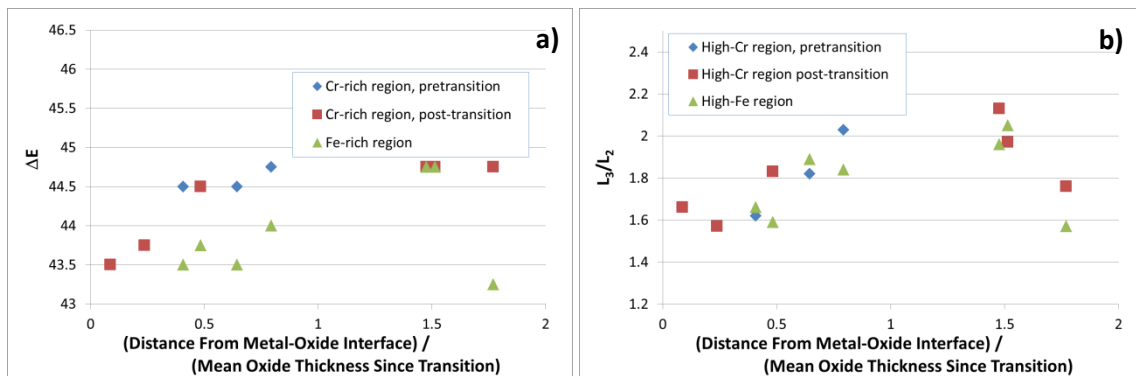


Figure 15 Change in oxidation state of Cr in cracks outside original SPP bounds using (a) ΔE (in eV) (b) L_3/L_2 .

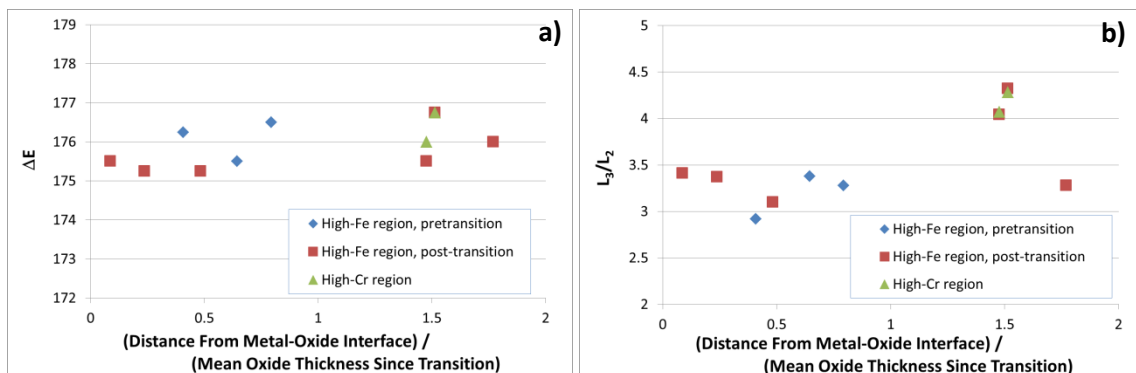


Figure 16 Change in oxidation state of Fe in cracks outside original SPP bounds using (a) ΔE (in eV) (b) L_3/L_2 .

Figure 16 indicates that the oxidation of Fe occurs very much later than that of Zr or Cr, with most oxidation probably occurring in the fossil oxide rather than in the part of the oxide growing in the current cycle. Thus, the fossil oxide is not completely inert.

Again, there is no difference between first cycle and second cycle behaviour in non-fossil parts of the oxide. Considering Figure 10 - Figure 16 together, there does not appear to be a step change in any characteristics of SPP oxidation at transition.

The cartoons in Figure 17 summarise the oxidation behaviour of the SPPs.

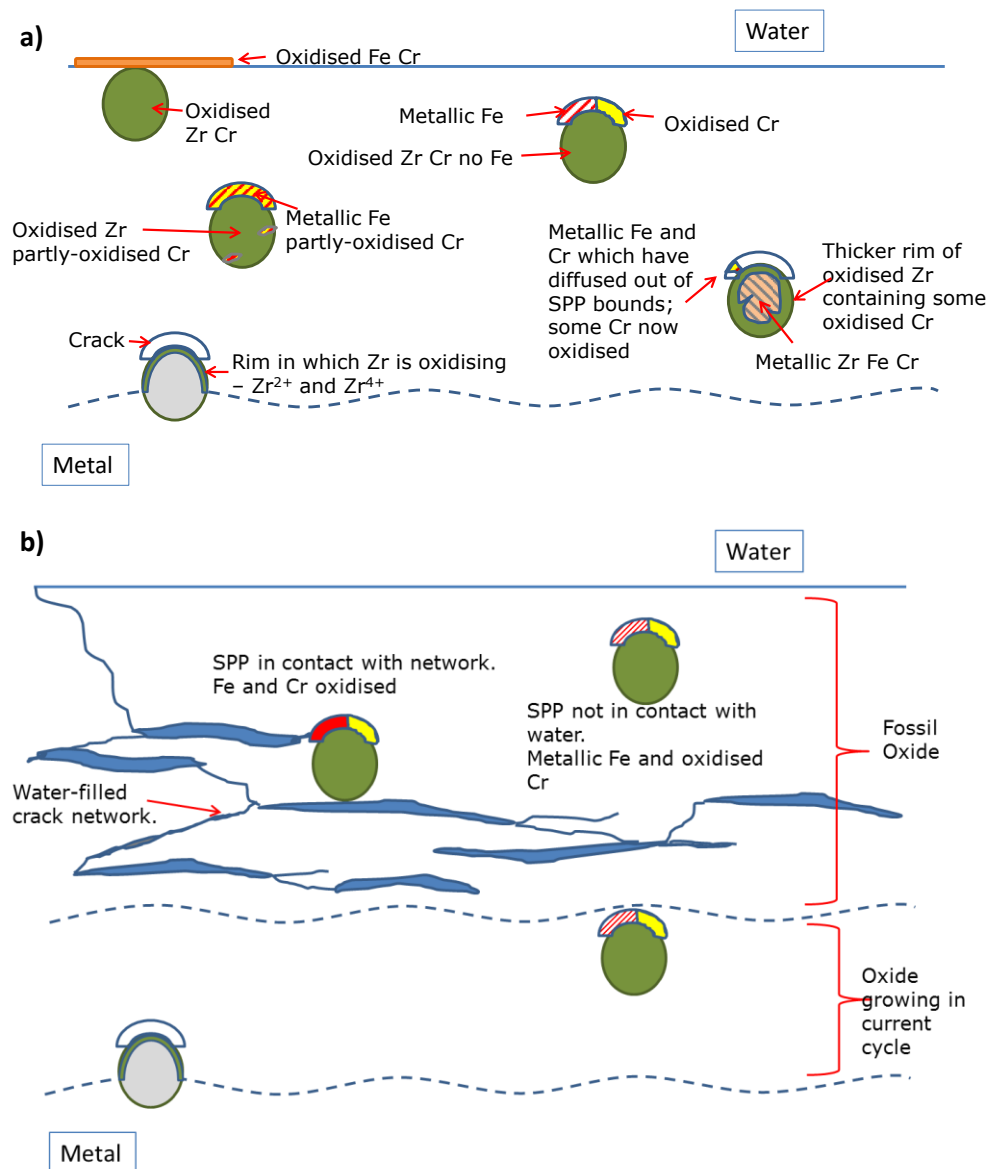


Figure 17. Summary of oxidation behaviour of SPPs. a) within oxide layer from current cycle (or pre-transition oxide) (b) within fossil oxide.

4. Discussion

The work presented here is more detailed than in previous examinations of SPP behaviour, and has been presented differently. In the following discussion we compare the information gained here with previous work to show that the trends observed are general. The various hypotheses concerning the role of SPPs in Zr alloy corrosion trends are then compared with the experimentally-observed trends in SPP oxidation to identify the most plausible hypotheses.

4.1 Comparison With Previous Work

The absolute magnitudes of the EELS parameters measured here are not exactly the same as those reported elsewhere in the literature [33] - [37]. This may be because the atomic /ionic environments in these samples are not quite the same as in the stoichiometric standards or because of differences in the way the data have been extracted. Under these circumstances, it is not possible to identify particular oxidation states for Fe and Cr at different locations across the oxides, although it is reasonable to assume that the asymptotic value reached in the fossil oxide represents the highest equilibrium oxidation state and the value in the substrate SPPs represents the metallic state.

Previous authors [27] [28] have shown that the overall level of oxidation in various SPPs increases with distance from the metal-oxide interface, but it can be difficult to correlate information from samples of different oxide thickness. The distance between the SPP and the MO affects the local oxygen potential (a thermodynamic effect) and also the time the SPP has been in contact with oxide (a kinetic effect). Considering the local oxygen potential in the oxide, the potential is expected to be lowest at the MO and highest at the OW. The OW, however, effectively shifts inwards at each transition in oxidation rates, with the oxygen potential expected to be fairly constant in the fossil oxide behind the new OW. Thus, the relation between SPP position and oxygen potential is not constant, and a location $1\mu\text{m}$ from the MO could be at the OW, half-way between the MO and the OW or in the fossil oxide in samples with $1\mu\text{m}$, $2\mu\text{m}$ or $2.5\mu\text{m}$ thick oxides respectively. The normalisation procedure in which the distance between the SPP location and the MO is divided by the mean oxide thickness grown since transition is intended to allow SPPs in different samples to be compared at similar oxygen potentials. The reproducibility of the data from the first and second cycles of oxidation indicates that this normalisation procedure captures the dominant factor in SPP oxidation.

Different authors have found Laves phase SPPs in Zircalloys to exhibit delayed oxidation with respect to the surrounding matrix or simultaneous oxidation, as summarised in [25]. The detailed study performed here may go some way to clarifying this apparent disagreement by showing the complexity of the overall oxidation process. For the Laves phase SPPs seen in the current work, Zr at the surface of the SPP begins to oxidise as the SPP crosses MO boundary. In this sense, there is no delay in oxidation. The Zr inside the SPP, however, oxidises progressively, with an intermediate level of oxidation found in an SPP at 90-250nm from the MO, and Zr oxidation remaining incomplete in an SPP found at 450nm from the MO. Collating the data on the normalised scale indicates that Zr oxidation is incomplete in Laves phase SPPs less than a quarter of the distance between the MO and OW.

The initial formation of a rim of oxidised Zr, and the progressive oxidation of the Zr in the SPPs will leave remnants of Laves phase to be observed within the oxide film, accounting for the observations of delayed SPP oxidation. This slow oxidation appears to be a kinetic effect, possibly related to the necessity for metallic Cr and Fe to migrate ahead of the oxidation front.

The migration of Fe ahead of the main MO into metallic Zr has been seen previously using atom probe tomography [39] [40]. The migration of Fe and Cr either ahead of the Zr oxidation front in SPPs or through ZrO_2 , has been seen on a number of previous occasions, with the metals collecting at SPP boundaries, in fissures in the SPPs, on the surfaces of cracks close to the SPPs or on the OW surface near the SPPs [14] [15] [25] [27] [28]. The Cr and Fe are expected to oxidise after the Zr, since their oxidation requires a higher partial pressure of oxygen, but this work has quantified their behaviour in terms of the oxide thickness. Cr begins to oxidise very close to the MO and is completely oxidised by around three quarters of the way across the oxide film, if the film is a pre-transition oxide, or three quarters of the way across the new oxide formed since transition for thicker oxides. Unexpectedly, Fe within the oxide film does not appear to oxidise fully before transition, and its oxidation state continues to increase even within the fossil oxide layer. This behaviour of the fossil layer is consistent with the observations of Pêcheur et al. [28] who found that the Fe expelled from SPPs at the water-oxide interface remained metallic on the surface of a $1\mu\text{m}$ oxide (3d exposure) formed on Zircaloy-4 in 400°C steam. Fe present on the surface for longer times (40d in the case of a $4\mu\text{m}$ oxide or 420d for a $14\mu\text{m}$ thick oxide) was oxidised. Even in direct contact with steam, then, the oxidation of the Fe islands requires some significant time. In the fossil oxide of a Zircaloy-4 sample exposed to 350°C water, some Fe islands will not be direct contact with the crack path bringing water to the MO, and full Fe oxidation will be further delayed. The oxidation of Fe is strongly affected by kinetic effects, and the fossil oxide is not completely inert.

If the oxidation of the elements in SPPs is kinetically limited, then the smaller the SPPs, the shorter the Fe and Cr diffusion distances, and the more rapidly the Zr can oxidise, the smaller the islands of Fe and Cr that can form in the surrounding cracks and, hence, the more rapidly these islands can oxidise. The smaller the SPPs, the more frequent, so again, the sooner the saturation oxidation level of Cr and Fe will develop in the ZrO_2 matrix. The destabilisation and destruction of SPPs under irradiation, and their replacement with ultrafine SPPs or islands of Fe would significantly reduce any kinetic delay in oxidising SPPs.

The thin film micro-beam X-ray absorption spectroscopy (μXANES) observations of Couet et al. [41] also support the possibility of kinetically-delayed Fe oxidation, in that they showed the fraction of oxidised Fe associated with two SPPs at similar distances from the metal-oxide interface of a $1.7\mu\text{m}$ thick oxide was lower in the larger SPP. They also showed that Fe in solid solution in the oxide was more highly oxidised than Fe in the SPPs, which may reflect the lack of a kinetic delay for dissolved Fe (although the possibility of the signal deriving from oxidised Fe picked up from the environment (the stainless steel autoclave) cannot be ignored). The thick-film μXANES observations do not agree so well with the observations here in that the Fe is deduced to begin to oxidise at smaller fractions of the oxide film thickness, and to reach 80% oxidation before transition. The difference in derived oxidation rates may be due to location averaging effects in the μXANES work (the beam FWHM was $0.2\mu\text{m} \times 0.2\mu\text{m}$ and the specimen thickness $200\mu\text{m}$), averaging over SPP and matrix oxidation states, fewer data points close to the metal-oxide interface than in the present work.

While the normalisation procedure used here makes it possible to compare data from samples of different thickness, it remains difficult to compare the current work with data from other studies without knowing the average oxide thicknesses at transition. When Annand et al. [27] examined Zr_2Fe and $\text{Zr}(\text{Fe,Cr})_2$ SPPs in Zircaloy-4 oxidised in high-pH water at 350°C , they found an approximately $0.7\mu\text{m}$ long Laves phase SPP “just inside the oxide scale” of a $2.96\mu\text{m}$ thick film. With

transition in this system occurring at around $2.2\mu\text{m}$ [42], the SPP probably spanned most of the oxide formed in the second oxidation cycle. Consistent with the current work, the Zr in this SPP did not appear to have oxidised entirely, especially close to the MO interface. A $0.6\mu\text{m}$ long SPP around $0.9\mu\text{m}$ from the MO in the $2.96\mu\text{m}$ film was probably mostly within the fossil oxide formed prior to transition. In this SPP the Cr and Zr appeared oxidised and the Fe partly oxidised and partly metallic. A Zr_2Fe particle $3\mu\text{m}$ from the MO in a $4.72\mu\text{m}$ oxide was probably entirely within the fossil oxide and was completely oxidised. The analysis of SPPs by De Gabory et al. [43] was less detailed, but the bright field imaging of a small SPP less than 5% of the way across a $1.9\mu\text{m}$ or $2\mu\text{m}$ thick (pretransition) oxide formed on Zircaloy-4 in 360°C water showed it to be unoxidised, at least in its centre, while a SPP around 40% of the way across appeared to be oxidised. The behaviour of each of the SPPs examined thus fits the trends shown in the present work. These consistent trends can therefore be used to consider the possible roles that the SPPs can play in oxidation and hydrogen pickup.

4.2 The Role Of SPPs

Considering first the contribution of SPPs in thin oxides, the EELS measurements have shown that Zr at the surface of the SPP begins to oxidise as the SPP crosses MO boundary. This makes it unlikely that the surface regions of an SPP stretching from the outer surface of an oxide film to the substrate will be metallic where it contacts the water i.e. the SPP, even while mainly metallic, will not act as a metallic bridge across the thin oxide film. Similarly, cathodic protection cannot be invoked if neither the substrate nor the SPP are in direct contact with the environment.

A metallic bridge could theoretically be produced even without metallic SPPs, if the metal migrating out of the SPPs produced a continuous layer crossing the oxide. The STEM/EELS study, however, suggests that both Fe and Cr prefer to cluster than to form extended features while in the metallic state. Some evidence also suggests that iron away from discrete islands oxidises more readily [41] than iron clustered in islands (in accordance with the kinetic basis suggested here for the delay in transition metal oxidation). Overall, forming and retaining a metallic grain boundary path crossing the oxide do not appear likely.

A continuous layer of transition metal oxide along grain boundaries would affect both oxidation rates and hydrogen pickup, and some observations of iron at oxide grain boundaries have been made with APT [44]. APT does not generally find iron in ZrO_2 grain boundaries, however [39] [40]. This may be because APT has investigated only oxide within about $0.5\mu\text{m}$ of the MO, at which position Fe migration out of the SPPs would be minimal. The EELS composition maps show no evidence of continuous layers of Fe oxide and, if Fe oxidation is heavily delayed, this seems an unlikely morphology to develop. In summary, while a variety of short-circuit paths can be envisaged, there is no direct evidence to support the existence of any metallic path or a path of either iron or chromium oxide across ZrO_2 : the proposed mechanisms by which Fe and Cr affect oxidation or hydrogen pickup which require short-circuit paths thus appear unlikely to operate.

Even without segregation, aliovalent doping of the bulk oxide is possible, with the non-Zr cation concentration increasing with distance from the MO. Some doping will result from the oxidation of the small amounts of Fe and Cr originally dissolved in the metal matrix or picked up from the

environment. The EELS data here show that doping from Cr cations originally within the SPPs can occur prior to transition. Once the Cr has oxidised. Doping from Fe will not occur until later. Further work would be required to measure diffusion profiles of Cr and Fe ions away from the oxidised islands around the SPPs and assess the contribution such delayed doping of the oxide might have on conductivity and diffusion-migration prior to transition.

The only mechanisms proposed to explain alloying element effects which have clear support from the present observation of oxides are those which involve islands of either iron oxide or metal. The increase in hydrogen pickup close to transition may relate to water beginning to percolate into the internal crack network [45], contacting metallic Fe and, in Zircaloy-2, metallic Ni. The metals may then catalyse the dissociation of hydrogen dissolved in the water within the crack network. Earlier in each cycle, islands of iron oxide will be formed mainly close to or on the outer surface (from Fe expelled from SPPs close to or intersecting the surface). Hole injection can then increase conductivity in the outermost part of the oxide. This might explain why decreasing the Fe:Cr ratio in SPPs decreases the corrosion rate [9].

The discussion to this point refers to the inter-transition corrosion rate, while SPPs have been found to affect transition or the onset of high, linear corrosion rates. No change was observed in the oxidation behaviour of Cr or Fe coincident with transition, suggesting that the role of SPPs is not to induce a conductivity-related transition. The influence of SPPs on transition is more likely to be related to mechanical rather than electrochemical effects, involving the influence of SPPs on plasticity or creep in the metal substrate [45] or on the tendency of the oxide to crack.

5. Summary And Conclusions

Mechanistic explanations of the role of SPPs in oxidation require support from microstructural observations. STEM/EELS measurements show that the oxidation of SPPs is a progressive process that is not complete before transition. The Zr on the rims of Laves phase SPPs begins to oxidise as the metal-oxide interface crosses the SPP, but is incomplete until the SPP is engulfed by the oxide and is around a quarter of the way between the metal-oxide interface and the oxide-water interface. The delay is probably related to the necessity for metallic Fe and Cr to migrate ahead of the oxidation front, and out of the original SPP bounds. The Cr is fully oxidised (change in oxidation state has reached a stable level) by the time the SPP is left around three quarters of the way between the metal-oxide interface and the oxide-water interface. By this time, the Fe has completely migrated outside the original SPP bounds. The Fe appears largely unoxidised prior to transition. No step change in oxidation state or element location is associated with transition.

The mechanisms which agree with these observations include: doping of the bulk ZrO_2 by low levels of aliovalent cations; doping ZrO_2 grain boundaries with aliovalent cations; injection of holes into near-surface oxide by islands of Fe_2O_3 ; reaction of water with islands of metallic Fe (and Ni) on surfaces of internal cracks around transition; control of transition by mechanical properties.

Acknowledgements

JS, SLP and SO are grateful to the National Nuclear Laboratory and the EPSRC for funding this work. The EPSRC (EP/K040375/1 and EP/N010868/1) is also acknowledged for funding the 'South of England Analytical Electron Microscope' and the FIB/SEM used in this research. The authors would like to thank Wood plc for the provision of autoclave facilities, CCFE for access to their TDS equipment and Oxford University for the provision of all other laboratory facilities. We are also grateful to Colin English and the many members of the MUZIC-2 consortium for their insights, information and helpful discussions.

References

- [1] H. G. Rickover, L. D. Geiger and B. Lustman, "History of the development of zirconium alloys for use in nuclear reactors. Report TID-26740," US Energy Research And Development Administration, 1975.
- [2] D. O. Northwood, "The development and applications of zirconium alloys," *Materials & Design*, vol. 6, no. 2, pp. 58-70, 1985.
- [3] G. P. Sabol, "ZIRLO(TM) - An alloy development success," in *Zirconium In The Nuclear Industry: 14th Int. Symp. ASTM STP 1467*, West Conshohocken, PA, USA, 2005.
- [4] Z. Duan, H. Yang, Y. Satoh, K. Murakami, S. Kano, Z. Zhao, J. Shen and H. Abe, "Current status of materials development of nuclear fuel cladding tubes for light water reactors," *Nuclear Engineering & Design*, vol. 316, pp. 131-150, 2017.
- [5] Y. Broy, F. Garzarolli, A. Seibold and L. F. Van Swam, "Influence of transition elements Fe, Cr and V on long-time corrosion in PWRs," in *Zirconium In The Nuclear Industry: 12th Int. Symp. ASTM STP 1354*, G. P. Sabol and G. D. Moan, Eds., West Conshohocken, ASTM, 2000, pp. 609-622.
- [6] B. Cox, "Some thoughts on the mechanisms of in-reactor corrosion of zirconium alloys," *J. Nuclear Mater.*, vol. 336, pp. 331-368, 2005.
- [7] P. Barberis, E. Ahlberg, N. Simic, D. Chrquet, C. Lemaignan, G. Wikmark, M. Dahlback, M. Limback, P. Tagstrom and B. Lehtinen, "Role of the second phase particles in zirconium binary alloys," in *Zirconium In The Nuclear Industry: 13th Int. Symp. ASTM STP 1423*, G. D. Moan and P. Rudling, Eds., West Conshohocken, PA: ASTM, 2002, pp. 33-58.
- [8] F. Garzarolli and H. Stehle, "Behaviour of structural materials for fuel and control elements in light water cooled power reactors," in *Improvements in water reactor fuel technology and performance*, Vienna, IAEA, 1987, pp. 387-407.
- [9] D. Charquet, "Microstructure and properties of zirconium alloys in the absence of irradiation," in *Zirconium In The Nuclear Industry: 12th Int. Symp. ASTM STP 1354*, G. P. Sabol and G. D. Moan, Eds., West Conshohocken, ASTM, 2000, pp. 3-14.

- [10] K. Kakiuchi, N. Itagaki, T. Furuya, A. Miyazaki, Y. Ishii, S. Suzuki, T. Terai and M. Yamawaki, "Role of iron for hydrogen absorption mechanism in zirconium alloys," in *Zirconium In The Nuclear Industry: 14th Int. Symp. ASTM STP 1467*, P. Rudling and B. Kammenzind, Eds., West Conshohocken, PA, USA, ASTM, 2004, pp. 349-366.
- [11] H. G. Weidinger, H. Ruhmann, G. Cheliotis, M. Maguire and T.-L. Yau, "Corrosion-electrochemical properties of zirconium intermetallics," in *Zirconium In The Nuclear Industry: 9th Int. Symp. ASTM STP 1132*, Philadelphia, USA, 1991.
- [12] H.-J. Beie, A. Mitwalsky, F. Garzarolli, H. Ruhmann and H.-J. Sell, "Examinations of the corrosion mechanism of zirconium alloys," in *Zirconium In The Nuclear Industry: 10th Int. Symp. ASTM STP 1245*, A. M. Garde and E. R. Bradley, Eds., Philadelphia, PA, USA, ASTM, 1994, pp. 615-643.
- [13] B. Cox, V. G. Kritsky, C. Lemaignan, V. Polley, I. G. Ritchie, H. Ruhmann, V. N. Shishov, Y. K. Bibilashvili and A. V. Nikulina, "Waterside Corrosion Of Zirconium Alloys In Nuclear Power Plants. IAEA-TECDOC-996," IAEA, Vienna, 1993.
- [14] T. Kubo and M. Uno, "Precipitate behaviour in Zircaloy-2 oxide films and its relevance to corrosion resistance," in *Zirconium In The Nuclear Industry: 9th Int. Symp. ASTM STP 1132*, Philadelphia, USA, 1991.
- [15] B. Cox and H. I. Sheikh, "Redistribution of the alloying elements during Zircaloy-2 oxidation," *J. Nuclear Mater.*, vol. 249, pp. 17-32, 1997.
- [16] P. Kofstad, "Chapter 2," in *High Temperature Corrosion*, UK, Elsevier Applied Science, 1988.
- [17] P. J. Shirvington and B. Cox, "A study of charge transport processes during the oxidation of zirconium alloys," *J. Nuclear Mater.*, vol. 35, pp. 211-222, 1970.
- [18] B. D. C. Bell, S. T. Murphy, P. A. Burr, R. W. Grimes and M. R. Wenman, "Accommodation of tin in tetragonal ZrO₂," *J. Appl. Phys.*, vol. 117, p. 084901, 2015.
- [19] B. Bell, S. Murphy, R. Grimes and M. Wenman, "The effect of Nb on the corrosion and hydrogen pickup of Zr alloys," *Acta Mater.*, vol. 132, pp. 425-431, 2017.
- [20] Y. R. Than, M. R. Wenman, B. D. C. Bell, S. R. Ortner, H. Swan and R. W. Grimes, "Modelling and experimental analysis of the effect of solute iron in thermally grown Zircaloy-4 oxides," *J. Nuclear Mater.*, vol. 509, pp. 114-123, 2018.
- [21] K. Kakiuchi, N. Itagaki, T. Furuya, A. Miyazaki, Y. Ishii, S. Suzuki, T. Terai and M. Yamawaki, "Role of iron for hydrogen absorption mechanism in zirconium alloys," *J. ASTM International.*, vol. 1, no. 10, p. JAI12352, 2004.
- [22] G. A. Eloff, C. J. Greyling and P. E. Viljoen, "The role of space charge in the oxidation of Zircaloy-4 between 350 and 450°C in air," *J. Nuclear Mater.*, vol. 199, pp. 285-288, 1993.

- [23] A. Couet, A. T. Motta and A. Ambard, "The coupled current charge compensation model for zirconium alloy fuel cladding oxidation: I. Parabolic oxidation of zirconium alloys," *Corr. Sci.*, vol. 100, pp. 73-84, 2015.
- [24] M. Lingren, G. Sundell, I. Panas, L. Hallstadius, M. Thuvander and H.-O. Andren, "Toward a comprehensive mechanistic understanding of hydrogen uptake in zirconium alloys by combining atom probe analysis with electronic structure calculations," in *Zirconium in the Nuclear Industry:17th Int. Symp., ASTM STP 1543*, Hyderabad, India, 2015.
- [25] C. Proff, S. Abolhassani and C. Lemaignan, "Oxidation behaviour of zirconium alloys and their precipitates - A mechanistic study," *J. Nuclear Mater.*, vol. 432, no. 1-2, pp. 222-238, 2013.
- [26] C. Proff, S. Abolhassani and C. Lemaignan, "Oxidation behaviour of binary zirconium alloys containing intermetallic precipitates," *J. Nuclear Mater.*, vol. 416, pp. 125-134, 2011.
- [27] K. Annand, M. Nord, I. MacLaren and M. Gass, "The corrosion of $Zr(Fe,Cr)_2$ and Zr_2Fe second phase particles in Zircaloy-4 under 350°C pressurised water conditions," *Corr. Sci.*, vol. 128, pp. 213-223, 2017.
- [28] D. Pecheur, F. Lefebvre, A. T. Motta, C. Lemaignan and J. F. Wadier, "Precipitate evolution in the Zircaloy-4 oxide layer," *J. Nuclear Mater.*, vol. 189, pp. 318-332, 1992.
- [29] D. Pecheur, F. Lefebvre, A. T. Motta, C. Lemaignan and D. Charquet, "Oxidation of intermetallic precipitates in Zircaloy-4: Impact of irradiation," in *Zirconium In The Nuclear Industry, 10th Int. Symp. ASTM STP 1245*, Philadelphia PA USA, ASTM, 1994, pp. 687-708.
- [30] D. J. Ives, *Principles of the extraction of metals*, London: The Royal Institute Of Chemistry, 1969.
- [31] *Standard Test method for Corrosion Testing of Products of Zirconium, Hafnium and their Alloys in Water at 680°F or in Steam at 750°F, ASTM G2/G2M-06*, ASTM, 2011.
- [32] J. Mayer, L. A. Gianuzzi, T. Kamino and J. Michael, "TEM sample preparation and damage," *MRS Bulletin*, vol. 32, pp. 400-407, 2007.
- [33] T. L. Daulton and B. J. Little, "Determination of chromium valence over the range Cr(0) - Cr(VI) by electron energy loss spectroscopy," *Ultramicroscopy*, vol. 106, pp. 561-573, 2006.
- [34] A. M. Arevalo-Lopez and M. A. Alario-Franco, "Reliable method for determining the oxidation state in chromium oxides," *Inorg. Chem.*, vol. 48, no. 24, pp. 11843-11846, 2009.
- [35] H. Tan, Verbeeck, A. Abakumov and G. Van Tendeloo, "Oxidation state and chemical shift investigation in transition metal oxides by EELS," *Ultramicroscopy*, vol. 116, pp. 24-33, 2012.
- [36] C. Colliex, T. Manoubi and C. ortiz, "Electron-energy-loss-spectroscopy near-edge fine structures in the iron-oxygen system," *Phys. Rev. B*, vol. 44, no. 20, pp. 11402-11411, 1991.

- [37] R. D. Leapman, L. A. Grunes and P. L. Fejes, "Study of the L23 edges in the 3d transition metals and their oxides by electron-energy-loss spectroscopy with comparisons to theory," *Phys. Rev. B*, vol. 26, no. 2, pp. 614-635, 1982.
- [38] J. Sayers, *Effect Of pH On Hydrogen Pickup And Corrosion Of Zircaloy-4*, D. Phil. Thesis, University Of Oxford, 2017.
- [39] G. Sundell, M. Thuvander and H.-O. Andren, "Barrier oxide chemistry and hydrogen pick-up mechanisms in zirconium alloys," *Corr. Sci.*, vol. 102, pp. 490-502, 2016.
- [40] Y. Dong, A. T. Motta and E. A. Marquis, "Atom probe tomography study of alloying element distributions in Zr alloys and their oxides," *J. Nuclear Mater.*, vol. 442, no. 1-3, pp. 270-281, 2013.
- [41] A. Couet, A. T. Motta, B. de Gabory and Z. Cai, "Microbeam X-ray absorption near-edge spectroscopy study of the oxidation of Fe and Nb in zirconium alloy oxide layers," *J. Nuclear Mater.*, vol. 452, pp. 614-627, 2014.
- [42] H. Swan, M. S. Blackmur, J. M. Hyde, A. LaFerrere, S. R. Ortner, P. D. Styman, C. Staines, M. Gass, H. Hulme, A. Cole-Baker and P. Frankel, "The measurement of stress and phase fraction distributions in pre and post-transition Zircaloy oxides using nano-beam synchrotron X-ray diffraction," *J. Nuclear Mater.*, vol. 479, pp. 559-575, 2016.
- [43] B. de Gabory, A. T. Motta and K. Wang, "Transition electron microscopy characterisation of Zircaloy-4 and ZIRLO oxide layers," *J. Nuclear Mater.*, vol. 456, pp. 272-280, 2015.
- [44] G. Sundell, M. Thuvander, A. K. Yatim, H. Nordin and H.-O. Andren, "Direct observation of hydrogen and deuterium in oxide grain boundaries in corroded zirconium alloys," *Corr. Sci.*, vol. 90, pp. 1-4, 2015.
- [45] S. Ortner, M. Blackmur, M. Fenwick, H. Weekes and M. Gass, "The role of metal plasticity in the growth of oxide on Zircaloy-4," in *Contribution of Materials Investigations and Operating Experience to Light Water NPPs' Safety, Performance and Reliability*, Avignon, France, 2018.
- [46] H. Tan, J. Verbeeck, A. Abakumov and G. Van Tendeloo, "Oxidation state and chemical shift investigation in transition metal oxides by EELS," *Ultramicroscopy*, vol. 116, pp. 24-33, 2012.
- [47] N. Ni, *Study of oxidation mechanisms of zirconium alloys by electron microscopy*, United Kingdom: Oxford University, 2011.
- [48] S. Lozano-Perez, "A guide on FIB preparation of samples containing stress corrosion crack tips for TEM and atom probe analysis," *Micron*, vol. 39, no. 3, pp. 320-328, 2008.
- [49] T. L. Daulton and B. J. Little, "Determination of chromium valence over the range Cr(0) - Cr(VI) by electron energy loss spectroscopy," *Ultramicroscopy*, vol. 106, pp. 561-573, 2006.

- [50] A. M. Arevalo-Lopez and M. A. Alario-Franco, "Reliable method for determining the oxidation state in chromium oxides," *Inorg. Chem.*, vol. 48, no. 24, pp. 11843-11846, 2009.
- [51] R. D. Leapman, L. A. Grunes and P. L. Fejes, "Study of the L23 edges in the 3d transition metals and their oxides by electron-energy-loss spectroscopy with comparisons to theory," *Phys. Rev. B*, vol. 26, no. 2, pp. 614-635, 1982.